SCIENCE CHINA
Physics, Mechanics & Astronomy

• Article •

March 2021 Vol. 64 No. 3: 237411
https://doi.org/10.1007/s11433-020-1626-3

Field-tuned magnetic structure and phase diagram of the honeycomb magnet $YbCl_3$

YiQing Hao[1†], HongLiang Wo[1†], YiMeng Gu[1], XiaoWen Zhang[1], YiQing Gu[1], ShiYi Zheng[1], Yang Zhao[2,3], GuangYong Xu[2], Jeffrey W. Lynn[2], Kenji Nakajima[4], Naoki Murai[4], WenBin Wang[5*], and Jun Zhao[1,6*]

[1]*State Key Laboratory of Surface Physics and Department of Physics, Fudan University, Shanghai 200433, China;*
[2]*NIST Center for Neutron Research, National Institute of Standards and Technology, Gaithersburg 20899, USA;*
[3]*Department of Materials Science and Engineering, University of Maryland, College Park 20742, USA;*
[4]*J-PARC Center, Japan Atomic Energy Agency (JAEA), Ibaraki 319-1195, Japan;*
[5]*Institute of Nanoelectronic Devices and Quantum Computing, Fudan University, Shanghai 200433, China;*
[6]*Collaborative Innovation Center of Advanced Microstructures, Nanjing 210093, China*

Received August 1, 2020; accepted October 12, 2020; published online December 31, 2020

We report thermodynamic and neutron diffraction measurements on the magnetic ordering properties of the honeycomb lattice magnet $YbCl_3$. We find $YbCl_3$ exhibits a Néel type long-range magnetic order at the wavevector (0, 0, 0) below T_N = 600 mK. This magnetic order is associated with a small sharp peak in heat capacity and most magnetic entropy release occurs above the magnetic ordering temperature. The magnetic moment lies in-plane, parallel to the monoclinic a-axis, whose magnitude m_{Yb} = 0.86(3) μ_B is considerably smaller than the expected fully ordered moment of 2.24 μ_B for the doublet crystal-field ground state. The magnetic ordering moment gradually increases with increasing magnetic field perpendicular to the ab-plane, reaching a maximum value of 1.6(2) μ_B at 4 T, before it is completely suppressed above ~ 9 T. These results indicate the presence of strong quantum fluctuations in $YbCl_3$.

magnetic order, neutron diffraction, honeycomb lattice

PACS number(s): 61.12.Ld, 75.25.+z, 75.30.-m, 76.30.Kg

Citation: Y. Q. Hao, H. L. Wo, Y. M. Gu, X. W. Zhang, Y. Q. Gu, S. Y. Zheng, Y. Zhao, G. Y. Xu, J. W. Lynn, K. Nakajima, N. Murai, W. B. Wang, and J. Zhao, Field-tuned magnetic structure and phase diagram of the honeycomb magnet $YbCl_3$, Sci. China-Phys. Mech. Astron. **64**, 237411 (2021), https://doi.org/10.1007/s11433-020-1626-3

1 Introduction

Frustrated magnets are materials where the magnetic interactions cannot be simultaneously fulfilled. These materials could exhibit novel states of magnetism, such as spin liquids or spin ices [1-4]. Magnetic frustration can be either induced by geometrical frustration [5-8], or by exchange frustration due to, e.g., Kitaev interactions on a honeycomb lattice. The Kitaev honeycomb model is exactly solvable with a quantum spin liquid ground state and emergent Majorana fermion excitations [9, 10]. For the long-sought realization of the Kitaev honeycomb model, abundant research efforts have been made on 4d/5d compounds, including α-$RuCl_3$, A_2IrO_3 (A = Na, Li, Cu) and $H_3LiIr_2O_6$, where strong spin-orbit coupling may give rise to Kitaev interactions [11-20]. While the zigzag magnetic order is the ground state in α-$RuCl_3$ and

*Corresponding authors (WenBin Wang, email: wangwb@fudan.edu.cn; Jun Zhao, email: zhaoj@fudan.edu.cn)
† These authors contributed equally to this work.

Na_2IrO_3 [21-25], the Kitaev quantum spin liquid (KQSL) behaviors have been revealed by various measurements in α-$RuCl_3$ [26-35] and $H_3LiIr_2O_6$ [20].

Theoretically, a J_1-J_2-J_3-K-Γ model has been developed to illustrate the magnetism in ruthenate and irridate materials [9, 36-42]. Here, the Heisenberg exchange interactions up to 3rd in-plane nearest neighbor (J_1, J_2 and J_3) need to be considered owing to the expansive nature of d-orbitals. K is the Kitaev interaction and Γ is the off-diagonal term enhanced by t_{2g}-e_g hopping [36]. For the pure Heisenberg model where only J_1, J_2 and J_3 exist, the competition among Heisenberg interactions can lead to a rich magnetic phase diagram including Néel, zigzag, and incommensurate magnetic ground states [40]. When the Kitaev interaction is included, the possible ground states of Néel, zigzag, stripe and ferromagnetic orders for different J_1/K ratio were also predicted [41]. Such a model was further enriched by adding off-diagonal terms of spin interactions in the system, introducing more complex phase diagrams [42].

Besides the intensively studied d-orbital compounds, it has been proposed that the rare earth compounds with strong spin-orbit coupling and anisotropic magnetic interactions may also exhibit Kitaev physics [43]. With much more localized 4f orbitals [44], the exchange interactions beyond the nearest neighbor (NN) bond can be neglected, simplifying the spin Hamiltonian. Following this line of thinking, $YbCl_3$ was suggested to be a candidate material for the Kitaev model [45]. Isostructural to α-$RuCl_3$, $YbCl_3$ is composed of 2D-honeycomb layers of Yb^{3+} ions coordinated in $YbCl_6$ octahedra. The crystal field splitting for 4f electrons of Yb^{3+} forms a Kramer's doublet where the ground state doublet is well isolated from excited crystal field levels [46]. Therefore, $YbCl_3$ can be considered as an effective spin-1/2 system. The heat capacity measurements in $YbCl_3$ revealed a large broad peak at around 1.2 K and a small sharp peak at 600 mK, which were attributed to short-range and long-range magnetic order, respectively [45]. Similar to α-$RuCl_3$, the anomalies in heat capacities are progressively suppressed by external field in $YbCl_3$. This implies that similar exotic magnetic correlations may exist in both systems. Indeed, recent inelastic neutron scattering measurements have revealed the coexistence of sharp spin wave and continuum excitations in $YbCl_3$ [47]. It is therefore particularly important to determine the microscopic magnetic structure of $YbCl_3$, which forms the basis where the exotic spin dynamics could be understood.

2 Experimental methods

High quality $YbCl_3$ single crystals were synthesized using the self-flux method from $YbCl_3$ powder (99.99%, Alfar Aesar). The starting material was first dehydrated at 250°C in the glove box and then sealed in the quartz tube under the vacuum. The sealed quartz tube was heated to 850°C in a tube furnace, and then cooled to 500°C in 150 h. Transparent single crystals with flat *ab*-surfaces were obtained. The neutron scattering experiments at zero field were performed on the BT-7 [48] and SPINS triple-axis spectrometers at the NIST Center for Neutron Research, Gaithersburg, Maryland, USA. The data were measured in the three-axis mode at both spectrometers. The neutron scattering experiment in magnetic field was performed on the AMATERAS [49] time-of-flight spectrometer at J-PARC, Tokai, Japan. For all three experiments, the sample was coated in Cytop to avoid hydrolysis before it was put in a ^{4}He cryostat with dilution insert and consequently cooled down to the base temperature of 60-80 mK. Heat capacity and AC susceptibility measurements were performed on single crystals from the same batch used for the neutron measurements using a Physical Property Measurement System (PPMS) from Quantum Design with ^{3}He-^{4}He dilution insert. The samples used in PPMS measurements were protected in N-grease.

3 Results and discussion

Figure 1(a) and (b) illustrate the crystal structure of $YbCl_3$. Isostructural to the KQSL material α-$RuCl_3$, $YbCl_3$ also adopts a slightly distorted honeycomb structure (space group $C2/m$). The lattice constants are a = 6.758 Å, b=11.617 Å, c = 6.335 Å with β = 110.7° at T = 1 K. The nearest Yb–Yb bond lengths in the *ab*-plane are 3.840 and 3.886 Å. Figure 1(c) and (d) show the heat capacity measurements under magnetic fields. At zero field, a small sharp peak indicative of a phase transition appears at T_N = 600 mK, whereas a broad peak indicating gradual entropy release is observed below 5 K. This is in agreement with ref. [45]. By applying magnetic field, T_N increased to ~800 mK at 2 T for in-plane magnetic field ($H//a$) and at 3 T for out-of-plane magnetic field ($H\perp ab$). As the magnetic field further increases, the sharp peak is completely suppressed at 7 T for $H//a$ and at 9 T for $H\perp ab$. The broad peak in heat capacity is also enhanced by a relatively small magnetic field, before it is fully suppressed at higher magnetic field (Figure 1(c) and (d)). These phase transitions are further confirmed by AC susceptibility measurements. As is shown in Figure 1(f), a sharp transition is observed at 6 T ($H//a$) at temperature of 0.1 and 0.4 K. As temperature increases, the peak observed in AC susceptibility becomes drastically broadened but is still visible for T = 1, 2 and 3 K. Figure 1(e) exhibits the DC-susceptibility measured between 2 and 300 K. The fitted Curie-Weiss temperature is Θ_{ab} = −4.9 K for $H//ab$ and $\Theta_{\perp}$ = −3.2 K for $H\perp ab$. These

results indicate dominant anti-ferromagnetic correlations in this material.

In order to determine the microscopic magnetic structure associated with the phase transitions seen in heat capacity and AC susceptibility in $YbCl_3$, we use neutron diffraction to measure the magnetic ordering properties of a single-crystalline sample. Figure 2(a)-(d) show elastic scans near several representative nuclear Bragg peak positions below and above T_N = 600 mK. It is revealed that the peak intensities are suppressed on warming from 80 mK to 1 K, indicative of a long-range magnetic order at **q** = (0, 0, 0). The intensity difference scan at (0, 4, 0) between 80 mK and 1 K shows a resolution-limited sharp peak, indicating that the order is long range in nature with a minimum correlation length of

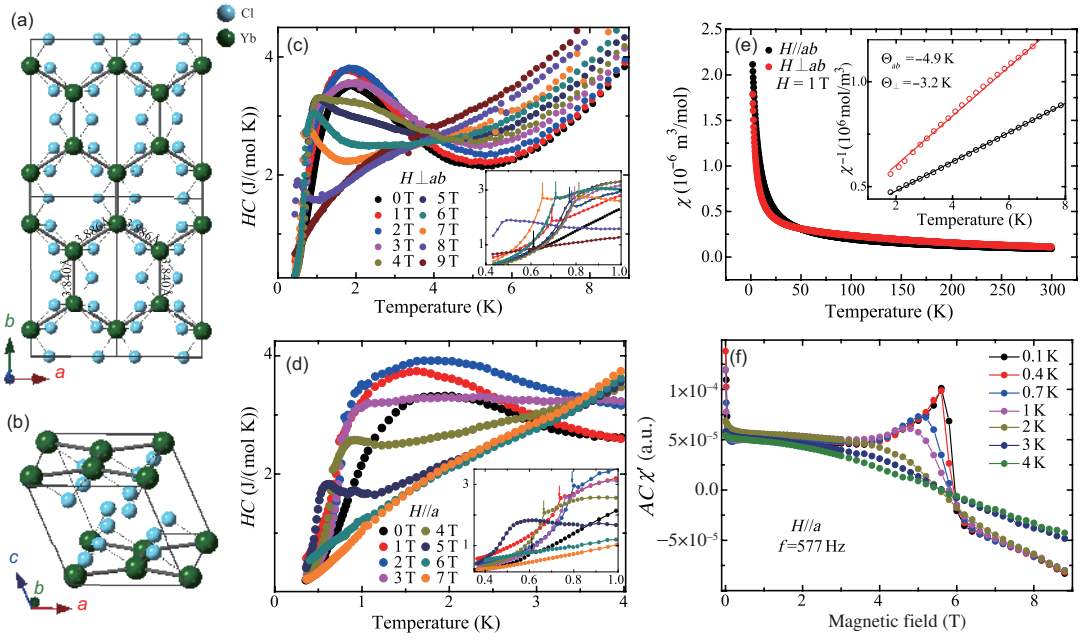

Figure 1 (Color online) (a), (b) Crystal structure of $YbCl_3$. Green and blue spheres represent Yb^{3+} ions and Cl^- anions, respectively; (c) heat capacity of $YbCl_3$ measured under magnetic field perpendicular to the *ab*-plane; (d) heat capacity of $YbCl_3$ measured under magnetic field parallel to the monoclinic *a*-axis. Inset of (c), (d) shows zoom-in of low temperature range. Arrows indicate phase transition temperatures at different magnetic fields. (e) DC-susceptibility of $YbCl_3$ measured between 2 K and 300 K. The magnetic fields were applied perpendicular (red dots) and parallel (black dots) to the *ab*-plane. Inset shows the fitting of Curie-Weiss temperature. (f) AC susceptibility of $YbCl_3$ measured under magnetic field parallel to the monoclinic *a*-axis.

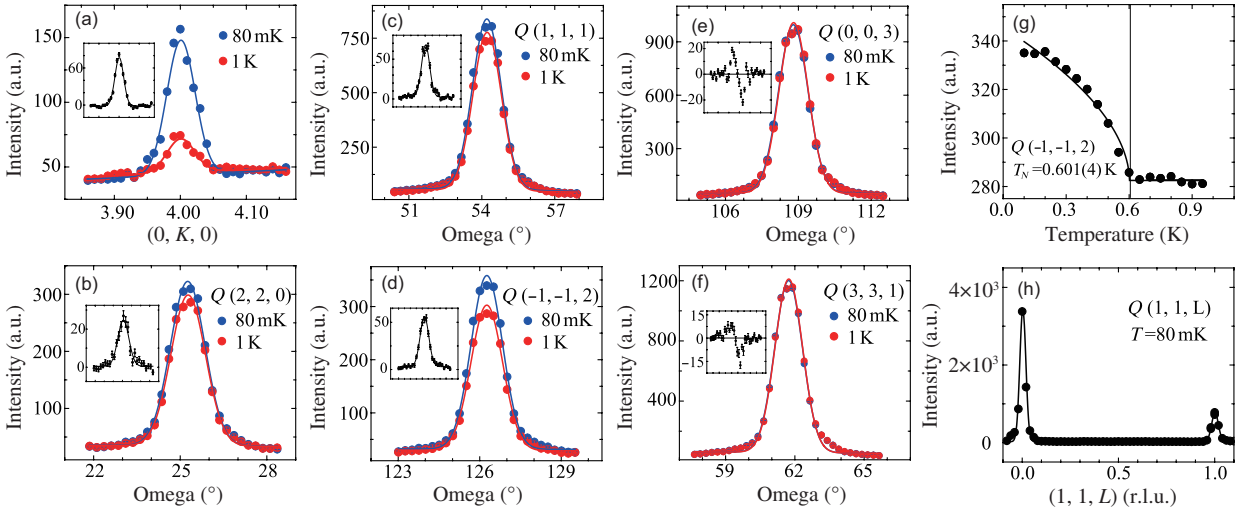

Figure 2 (Color online) (a) *K*-scan near the (0, 4, 0) Bragg peak position at 80 mK and 1 K measured on SPINS. (b)-(f) Rocking scans measured in (HHL) plane on BT-7 near the indicated Bragg peak positions. Blue and red dots indicate neutron diffraction intensity at 80 mK and 1 K, respectively. Insets show the intensity difference between 80 mK and 1 K. Solid lines were fits using a Gaussian function. (g) Temperature dependence of (–1, –1, 2) magnetic Bragg peak measured at BT-7. Solid line represents a fit using the power-law function $I-I_0 \propto (1-T/T_N)^{2\beta}$. The vertical line indicating the fitted Néel temperature of 0.601(4) K. (h) *L*-scan measured from the (1, 1, 0) to (1, 1, 1) Bragg peaks at 80 mK. Error bars (in some cases smaller than the symbols) indicate 1 standard deviation.

228(8) Å (Figure 2(a)). The detailed temperature dependence of the intensity of the (1, 1, –2) Bragg peak shows a continuous phase transition, which can be fitted by the power-law function $I-I_0 \propto (1-T/T_N)^{2\beta}$ with a critical exponent of β = 0.265(23) (Figure 2(g)). The fit yields a Néel temperature of T_N = 601(4) mK, consistent with the sharp anomalies seen in heat capacity measurements. For the magnetic structure refinements, 37 neutron diffraction peaks were collected in the (HHL) plane, at both 80 mK and 1 K. Except for K = 0 and K = 3 Bragg peaks (Figure 2(e) and (f) as the representative), all measured Bragg peaks exhibit different intensity below and above T_N. This strongly implies that $YbCl_3$ exhibits a Néel-type antiferromagnetic order. Figure 2(h) shows an L-scan measured near (1, 1, 0) and (1, 1, 1), no satellite peaks at L = 1/2 or 1/3 are observed, indicating that the sample is a single domain without stacking order. Such stacking order is commonly seen in α-$RuCl_3$ [22].

Figure 3 summarizes the integrated intensity difference between 80 mK and 1 K of representative Bragg peaks. A total of 15 peaks in (HHL) plane with clear magnetic intensities

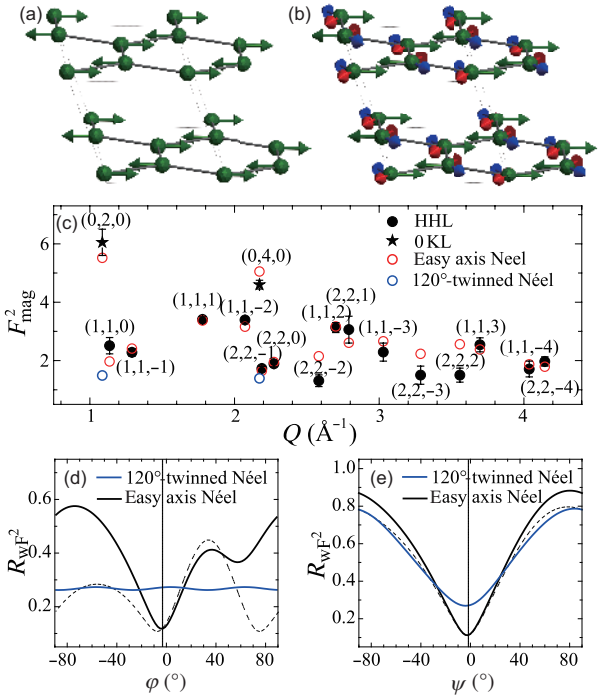

Figure 3 (Color online) Schematic diagrams of (a) a-axis Néel order of $YbCl_3$ and (b) 120°-twinned Néel orders of $YbCl_3$. Red, blue and green arrows demonstrate the magnetic moments for a single twin respectively. (c) Magnetic refinement of $YbCl_3$ for both a-axis Néel and 120°-twinned Néel models. Filled circles indicate experimental data in the (HHL) plane at BT-7, while filled stars indicate the (0KL) peaks collected at SPINS. Red and blue open circles represent the calculation for single easy-axis Néel and 120°-twinned Néel models, respectively. (d), (e) Weighed R-factor by spin direction angles φ and ψ defined in the main text. Black and blue solid lines illustrate the fitting for single easy-axis and 120°-twinned models respectively, and the dashed line shows the fitting for the single easy-axis model using only (HHL) magnetic peaks.

were included in refinements using Fullprof software suite [50]. Unrestrained least squares fitting gives the magnetic moments M_a = 0.86(3) μ_B, M_b = –0.04(3) μ_B and M_c = –0.02(3) μ_B (R_{wp} = 11.1%). This indicates a Néel-type magnetic order with the moment along the a-axis, as is illustrated in Figure 3(a). It should be noted that a 3-twinned magnetic structure (Figure 3(b)) can give an equal fit to the peaks in (HHL) plane. Nevertheless, the (0, 2, 0) and (0, 4, 0) peaks measured at SPINS strongly favor the single easy-axis structure over the 120°-twinned one, as is shown in Figure 3(c). Figure 3(d) and (e) show the weighted R-factor by different moment directions, where φ is the angle between easy-axis and a-axis in ab-plane and ψ is the angle between easy-axis and a-axis in ac-plane. It is shown that, when considering (HHL) and (0KL) diffraction peaks, best fitting quality is achieved assuming a single easy-axis along the monoclinic a-axis. The fitted angle between the magnetic easy axis and a-axis is –2(3) degrees in the ac-plane.

The easy-axis Néel magnetic structure suggests the existence of anisotropy within the honeycomb ab-plane. This is understandable as the structure of $YbCl_3$ exhibits a slight distortion (~1%) away from the perfect honeycomb lattice. The distortion of the $YbCl_6$ octahedron may in turn affect the crystal fields that lead to the in-plane anisotropy. The observation of a Néel-type order puts constraints on the spin Hamiltonian that describes the magnetism in this system. For the Heisenberg model, the Néel state is favored when $J_1 > 0$ and $J_2 < 0$ [40]. For the Heisenberg-Kitaev model, $K > 0$, $J > 0$ and $K < 0$, $J > 0$ can both lead to the Néel state [41]. In $YbCl_3$, the magnetic moment m = 0.86(3) μ_B is considerably smaller than the expected fully ordered moment of 2.24 μ_B for the doublet CEF ground state [46]. This indicates strong quantum fluctuation in the system, as is also implied in the heat capacity measurements, where a large part of the magnetic entropy release occurs above the magnetic ordering temperature. It is therefore possible that Kitaev or off-diagonal term exists in the spin Hamiltonian, which introduces exchange frustration in the system.

To further elucidate the effect of magnetic fields on the phase transitions seen in heat capacity and susceptibility measurements (Figure 1), we use neutron scattering to measure the magnetic structure of $YbCl_3$ in magnetic fields. Figure 4(a) and (b) show (1, 3, 0) and (0, 4, 0) Bragg peaks in zero field and 4 T field applied perpendicular to the ab-plane. A clear enhancement of neutron diffraction intensity is observed at 4 T in both Bragg peaks. Since K = 3 is disallowed in the Néel-type magnetic order, this result strongly suggests the presence of canted moments in magnetic fields. Figure 4(c) summarizes the integrated intensity of (0, 2, 0), (0, 4, 0) and (1, 3, 0) Bragg peaks at 0, 2, 3, and 4 T. The corresponding magnetic structures are fitted assuming a canted magnetic or-

der with the Néel component along the *a*-axis and ferromagnetic component perpendicular to the *ab*-plane (inset of Figure 4(d)). The estimated magnetic moments are summarized in Table 1. It is shown that the magnetic ordering moment increases with increasing field from 0 to 4 T. In the meantime, the Néel temperature increases from 600 mK at zero field to 800 mK at 4 T. These results suggest that a relatively low magnetic field would suppress the quantum fluctuation and enhance the magnetic order.

4 Conclusions

To summarize, we have shown that the small sharp heat capacity peak at T_N = 600 mK in $YbCl_3$ is due to the Néel-type magnetic order with the moment pointing along the monoclinic *a*-axis. In magnetic fields perpendicular to the *ab*-plane, the magnetic structure is canted and the moment increases from 0.86(3) μ_B at 0 T to 1.6(2) μ_B at 4 T. T_N increases to 800 mK at 4 T before decreasing again at higher fields (Figure 4(d)). In magnetic fields along the easy *a*-axis, T_N is enhanced to 800 mK at 2 T before it is fully suppressed at 6 T (Figure 4(e)). The fact that m_{Yb} = 0.86(3) μ_B at zero field is much smaller than the expected fully ordered moment of 2.24 μ_B together with the tiny magnetic entropy release correlated with the order indicates the presence of strong quantum fluctuations in $YbCl_3$. The precise determination of the magnetic structure and its field evolution provide the basis from which a microscopic theory can be established to understand the exotic spin correlations in this system.

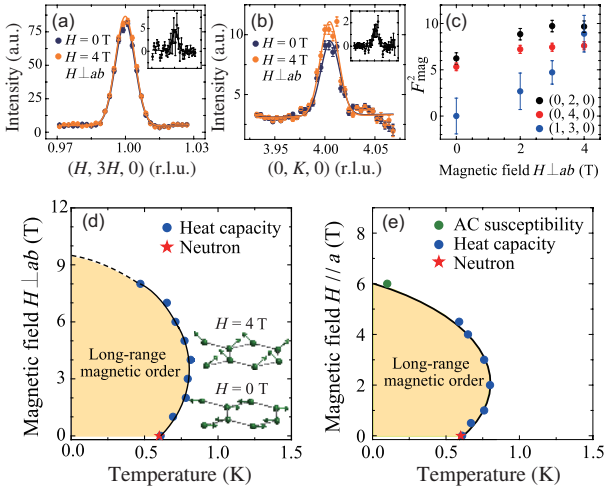

Figure 4 (Color online) (a), (b) (1, 3, 0) and (0, 4, 0) Bragg peaks measured at 60 mK on AMATERAS, the magnetic field is applied perpendicular to the *ab*-plane. Blue and orange dots indicate neutron diffraction intensities at 0 and 4 T, respectively. The insets show the subtractions between 0 and 4 T. (c) Integrated neutron diffraction intensity of (0, 2, 0), (0, 4, 0) and (1, 3, 0) Bragg peaks from 0 to 4 T. (d), (e) Field-temperature magnetic phase diagrams of $YbCl_3$. Green and blue dots are determined from the AC susceptibility and heat capacity measurements in the present work (Figure 1(c), (d) and (f)). Red star is determined by our neutron diffraction results (Figure 2(g)). The magnetic field is applied perpendicular to the *ab*-plane (d) and parallel to the easy *a*-axis (e), respectively. Insets of (d) show models of magnetic structure at 0 and 4 T. Error bars indicate 1 standard deviation.

Table 1 Magnetic moments of $YbCl_3$ in field perpendicular to the *ab*-plane

Field (T) $H \perp ab$	$\mathbf{M}_a$ (μ_B) Néel	$\mathbf{M}_\perp$ (μ_B) FM	$\mathbf{M}_{Yb}$ (μ_B) total
0	0.86(3)	0	0.86(3)
2	1.0(2)	0.4(19)	1.1(2)
3	1.0(2)	0.57(15)	1.2(2)
4	0.94(16)	0.86(14)	1.6(2)

Note added: During the submission of this manuscript, we became aware of a related neutron diffraction work reporting the magnetic structure of $YbCl_3$ in zero field [51]. In ref. [51], the angle between the magnetic easy-axis and *a*-axis is 16(11) degrees which is sligtly different from that (–2(3) degrees) obtained in current work in zero field. The magnetic moment 0.8(1) μ_B in ref. [51] is also slightly smaller than that (0.86(3) μ_B) in this work.

This work was supported by the National Key R&D Program of the Ministry of Science and Technology of China (Grant No. 2016YFA0300203), the Innovation Program of Shanghai Municipal Education Commission (Grant No. 2017-01-07-00-07-E00018), the Shanghai Municipal Science and Technology Major Project (Grant No. 2019SHZDZX01), and the National Natural Science Foundation of China (Grant No. 11874119). The identification of any commercial product or trade name does not imply endorsement or recommendation by the National Institute of Standards and Technology. The neutron experiment at the Materials and Life Science Experimental Facility of the J-PARC was performed under a user program (Proposal No. 2019B0262).

1 L. Balents, Nature **464**, 199 (2010).
2 X. G. Wen, Phys. Rev. B **65**, 165113 (2002), arXiv: cond-mat/0107071.
3 Y. Zhou, K. Kanoda, and T. K. Ng, Rev. Mod. Phys. **89**, 025003 (2017), arXiv: 1607.03228.
4 S. T. Bramwell, and M. J. P. Gingras, Science **294**, 1495 (2001), arXiv: cond-mat/0201427.
5 P. W. Anderson, Mater. Res. Bull. **8**, 153 (1973).
6 T. H. Han, J. S. Helton, S. Chu, D. G. Nocera, J. A. Rodriguez-Rivera, C. Broholm, and Y. S. Lee, Nature **492**, 406 (2012), arXiv: 1307.5047.
7 Y. Shen, Y. D. Li, H. Wo, Y. Li, S. Shen, B. Pan, Q. Wang, H. C. Walker, P. Steffens, M. Boehm, Y. Hao, D. L. Quintero-Castro, L. W. Harriger, M. D. Frontzek, L. Hao, S. Meng, Q. Zhang, G. Chen, and J. Zhao, Nature **540**, 559 (2016), arXiv: 1607.02615.
8 W. Liu, Z. Zhang, J. Ji, Y. Liu, J. Li, X. Wang, H. Lei, G. Chen, and Q. Zhang, Chin. Phys. Lett. **35**, 117501 (2018), arXiv: 1809.03025.
9 A. Kitaev, Ann. Phys. **321**, 2 (2006), arXiv: cond-mat/0506438.
10 G. Jackeli, and G. Khaliullin, Phys. Rev. Lett. **102**, 017205 (2009), arXiv: 0809.4658.
11 K. W. Plumb, J. P. Clancy, L. J. Sandilands, V. V. Shankar, Y. F. Hu, K. S. Burch, H. Y. Kee, and Y. J. Kim, Phys. Rev. B **90**, 041112 (2014), arXiv: 1403.0883.
12 M. Majumder, M. Schmidt, H. Rosner, A. A. Tsirlin, H. Yasuoka, and M. Baenitz, Phys. Rev. B **91**, 180401 (2015), arXiv: 1411.6515.
13 Y. Singh, and P. Gegenwart, Phys. Rev. B **82**, 064412 (2010).

14 J. Chaloupka, G. Jackeli, and G. Khaliullin, Phys. Rev. Lett. **105**, 027204 (2010), arXiv: 1004.2964.
15 Y. Singh, S. Manni, J. Reuther, T. Berlijn, R. Thomale, W. Ku, S. Trebst, and P. Gegenwart, Phys. Rev. Lett. **108**, 127203 (2012), arXiv: 1106.0429.
16 S. Hwan Chun, J. W. Kim, J. Kim, H. Zheng, C. C. Stoumpos, C. D. Malliakas, J. F. Mitchell, K. Mehlawat, Y. Singh, Y. Choi, T. Gog, A. Al-Zein, M. M. Sala, M. Krisch, J. Chaloupka, G. Jackeli, G. Khaliullin, and B. J. Kim, Nat. Phys. **11**, 462 (2015).
17 M. Abramchuk, C. Ozsoy-Keskinbora, J. W. Krizan, K. R. Metz, D. C. Bell, and F. Tafti, J. Am. Chem. Soc. **139**, 15371 (2017).
18 S. K. Takahashi, J. Wang, A. Arsenault, T. Imai, M. Abramchuk, F. Tafti, and P. M. Singer, Phys. Rev. X **9**, 031047 (2019).
19 J. Knolle, R. Moessner, and N. B. Perkins, Phys. Rev. Lett. **122**, 047202 (2019).
20 K. Kitagawa, T. Takayama, Y. Matsumoto, A. Kato, R. Takano, Y. Kishimoto, S. Bette, R. Dinnebier, G. Jackeli, and H. Takagi, Nature **554**, 341 (2018).
21 J. A. Sears, M. Songvilay, K. W. Plumb, J. P. Clancy, Y. Qiu, Y. Zhao, D. Parshall, and Y. J. Kim, Phys. Rev. B **91**, 144420 (2015), arXiv: 1411.4610.
22 R. D. Johnson, S. C. Williams, A. A. Haghighirad, J. Singleton, V. Zapf, P. Manuel, I. I. Mazin, Y. Li, H. O. Jeschke, R. Valentì, and R. Coldea, Phys. Rev. B **92**, 235119 (2015), arXiv: 1509.02670.
23 H. B. Cao, A. Banerjee, J. Q. Yan, C. A. Bridges, M. D. Lumsden, D. G. Mandrus, D. A. Tennant, B. C. Chakoumakos, and S. E. Nagler, Phys. Rev. B **93**, 134423 (2016), arXiv: 1602.08112.
24 X. Liu, T. Berlijn, W. G. Yin, W. Ku, A. Tsvelik, Y. J. Kim, H. Gretarsson, Y. Singh, P. Gegenwart, and J. P. Hill, Phys. Rev. B **83**, 220403 (2011), arXiv: 1104.4046.
25 F. Ye, S. Chi, H. Cao, B. C. Chakoumakos, J. A. Fernandez-Baca, R. Custelcean, T. F. Qi, O. B. Korneta, and G. Cao, Phys. Rev. B **85**, 180403 (2012), arXiv: 1202.3995.
26 A. Banerjee, C. A. Bridges, J. Q. Yan, A. A. Aczel, L. Li, M. B. Stone, G. E. Granroth, M. D. Lumsden, Y. Yiu, J. Knolle, S. Bhattacharjee, D. L. Kovrizhin, R. Moessner, D. A. Tennant, D. G. Mandrus, and S. E. Nagler, Nat. Mater. **15**, 733 (2016), arXiv: 1504.08037.
27 A. Banerjee, J. Yan, J. Knolle, C. A. Bridges, M. B. Stone, M. D. Lumsden, D. G. Mandrus, D. A. Tennant, R. Moessner, and S. E. Nagler, Science **356**, 1055 (2017).
28 S. H. Baek, S. H. Do, K. Y. Choi, Y. S. Kwon, A. U. B. Wolter, S. Nishimoto, J. van den Brink, and B. Büchner, Phys. Rev. Lett. **119**, 037201 (2017), arXiv: 1702.01671.
29 Y. Kasahara, T. Ohnishi, Y. Mizukami, O. Tanaka, S. Ma, K. Sugii, N. Kurita, H. Tanaka, J. Nasu, Y. Motome, T. Shibauchi, and Y. Matsuda, Nature **559**, 227 (2018), arXiv: 1805.05022.
30 R. Hentrich, M. Roslova, A. Isaeva, T. Doert, W. Brenig, B. Büchner, and C. Hess, Phys. Rev. B **99**, 085136 (2019), arXiv: 1803.08162.
31 D. Hirobe, M. Sato, Y. Shiomi, H. Tanaka, and E. Saitoh, Phys. Rev. B **95**, 241112 (2017), arXiv: 1611.04799.
32 S. H. Do, S. Y. Park, J. Yoshitake, J. Nasu, Y. Motome, Y. S. Kwon, D. T. Adroja, D. J. Voneshen, K. Kim, T. H. Jang, J. H. Park, K. Y. Choi, and S. Ji, Nat. Phys. **13**, 1079 (2017).
33 I. A. Leahy, C. A. Pocs, P. E. Siegfried, D. Graf, S. H. Do, K. Y. Choi, B. Normand, and M. Lee, Phys. Rev. Lett. **118**, 187203 (2017), arXiv: 1612.03881.
34 L. J. Sandilands, Y. Tian, K. W. Plumb, Y. J. Kim, and K. S. Burch, Phys. Rev. Lett. **114**, 147201 (2015), arXiv: 1504.05202.
35 Z. Wang, S. Reschke, D. Hüvonen, S. H. Do, K. Y. Choi, M. Gensch, U. Nagel, T. Rõõm, and A. Loidl, Phys. Rev. Lett. **119**, 227202 (2017), arXiv: 1706.06157.
36 W. Wang, Z. Y. Dong, S. L. Yu, and J. X. Li, Phys. Rev. B **96**, 115103 (2017), arXiv: 1612.09515.
37 T. Suzuki, and S. Suga, Phys. Rev. B **97**, 134424 (2018), arXiv: 1802.00545.
38 Y. F. Jiang, T. P. Devereaux, and H. C. Jiang, Phys. Rev. B **100**, 165123 (2019), arXiv: 1901.09131.
39 K. Ran, J. Wang, W. Wang, Z. Y. Dong, X. Ren, S. Bao, S. Li, Z. Ma, Y. Gan, Y. Zhang, J. T. Park, G. Deng, S. Danilkin, S. L. Yu, J. X. Li, and J. Wen, Phys. Rev. Lett. **118**, 107203 (2017), arXiv: 1702.04920.
40 D. C. Cabra, C. A. Lamas, and H. D. Rosales, Phys. Rev. B **83**, 094506 (2011), arXiv: 1003.3226.
41 J. Chaloupka, G. Jackeli, and G. Khaliullin, Phys. Rev. Lett. **110**, 097204 (2013), arXiv: 1209.5100.
42 J. G. Rau, E. K. H. Lee, and H. Y. Kee, Phys. Rev. Lett. **112**, 077204 (2014), arXiv: 1310.7940.
43 Z.-X. Luo, and G. Chen, arXiv: 1903.02530v3.
44 F. Y. Li, Y. D. Li, Y. Yu, A. Paramekanti, and G. Chen, Phys. Rev. B **95**, 085132 (2017), arXiv: 1607.05618.
45 J. Xing, H. Cao, E. Emmanouilidou, C. Hu, J. Liu, D. Graf, A. P. Ramirez, G. Chen, and N. Ni, arXiv: 1903.03615v1.
46 G. Sala, M. B. Stone, B. K. Rai, A. F. May, D. S. Parker, G. B. Halász, Y. Q. Cheng, G. Ehlers, V. O. Garlea, Q. Zhang, M. D. Lumsden, and A. D. Christianson, Phys. Rev. B **100**, 180406 (2019), arXiv: 1907.10627.
47 G. Sala, M. B. Stone, B. K. Rai, A. F. May, P. Laurell, V. O. Garlea, N. P. Butch, M. D. Lumsden, G. Ehlers, G. Pokharel, D. Mandrus, D. S. Parker, S. Okamoto, G. B. Halász, and A. D. Christianson, arXiv: 2003.01754v1.
48 J. W. Lynn, Y. Chen, S. Chang, Y. Zhao, S. Chi, W. Ratcliff II, B. G. Ueland, and R. W. Erwin, J. Res. Natl. Inst. Stand. Technol. **117**, 60 (2012).
49 K. Nakajima, S. Ohira-Kawamura, T. Kikuchi, M. Nakamura, R. Kajimoto, Y. Inamura, N. Takahashi, K. Aizawa, K. Suzuya, K. Shibata, T. Nakatani, K. Soyama, R. Maruyama, H. Tanaka, W. Kambara, T. Iwahashi, Y. Itoh, T. Osakabe, S. Wakimoto, K. Kakurai, F. Maekawa, M. Harada, K. Oikawa, R. E. Lechner, F. Mezei, and M. Arai, J. Phys. Soc. Jpn. **80**, SB028 (2011).
50 J. Rodrìguez-Carvajal, Physica B-Condens. Matter **192**, 55 (1993).
51 J. Xing, E. Feng, Y. Liu, E. Emmanouilidou, C. Hu, J. Liu, D. Graf, A. P. Ramirez, G. Chen, H. Cao, and N. Ni, Phys. Rev. B **102**, 014427 (2020).